Supplement of Atmos. Chem. Phys., 23, 6487–6523, 2023
https://doi.org/10.5194/acp-23-6487-2023-supplement

Supplement of

A new process-based and scale-aware desert dust emission scheme for global climate models – Part I: Description and evaluation against inverse modeling emissions

Danny M. Leung et al.

Correspondence to: Danny M. Leung (dannymleung@ucla.edu)

Section S1. Converting the volumetric soil moisture to the gravimetric soil moisture.

The conversion from volumetric to gravimetric soil moisture is documented in many papers, such as in Oleson et al. (2013). We followed Kok et al. (2014b) and adopted a globally constant soil particle density of $\rho_p = 2650$ kg m^{-3}. Then we used the MERRA-2 global soil porosity (poros, φ, Fig. S1b) to yield the bulk density of soil ρ_b:

$$\rho_b = \rho_p(1 - \varphi) \qquad \text{(S1)}$$

Then, using the water density of $\rho_w = 1000$ kg m^{-3}, we converted the MERRA-2 volumetric soil moisture (SFMC, θ, m^3 water / m^3 soil, Fig. S1a) to gravimetric moisture w (kg water / kg soil, Fig. S1c):

$$w = \frac{\rho_w}{\rho_b}\theta \qquad \text{(S2)}$$

Section S2. A discussion on other approaches of combining rock and vegetation drag partition effects

To our knowledge only a few approaches explicitly proposed to represent both rock and vegetation roughness in one drag partition scheme, but they all have different limitations. The first approach was proposed by Darmenova et al. (2009) and subsequently modified by Foroutan et al. (2017): They assumed rock λ for different land types (e.g., Table 2 in Darmenova et al., 2009), and combined rock λ with vegetation λ (from Eq. 9b) using Darmenova's double drag partition equation (see Eq. 5 in Foroutan et al., 2017). The second approach was also proposed by Darmenova et al. (2009): They provided measured rock z_{0a} and vegetation z_{0a} for different land types (Table 1 in Darmenova et al., 2009), determined the dominant land type (bare or vegetated) for each grid, and then applied M&B95 to calculate drag partitioning. The third approach was proposed by Klose et al. (2021): They provided a relation between vegetation λ, h, and z_{0a}, plus a relation between vegetation height h and LAI, and thus derived the vegetation roughness length z_{0a} as a function of LAI. They then used Prigent et al. (2012) satellite measurements of z_{0a} (time-invariant, static, mostly representing rocks), and took the larger z_{0a} between Prigent's static z_{0a} and their dynamic vegetation z_{0a}. They finally used M&B95 to calculate drag partitioning with z_{0a}. All three approaches tried to represent both rock and vegetation roughness using either z_{0a} or λ, which was problematic because rocks are better measured in z_{0a} by satellites and plants are better parameterized in λ. For example, globally gridded rock λ was not available and thus the first and second approaches needed to assign λ for rocks as a function of land type, which can be inaccurate and highly uncertain because λ also depends on other factors apart from the land type. On the other hand, the second and the third approaches assumed one dominant land type and used one single (either rock or vegetation) z_{0a} to represent the whole grid, but ignored the fact that a grid can be partly covered by plants and partly by rocks, which was only accounted for by the first approach (the double drag partition equation is a function of rock λ, plant λ, and f_v). Note that the second and the third approaches had to choose either rock or plant z_{0a} because adding up the rock z_{0a} and plant z_{0a} is not allowed (z_0 is not additive, whereas λ is additive). The same problem would not occur if there were global scale observations of rock roughness measured in density λ, which could either be directly applied to the double drag partition equation in Darmenova et al. (2009) or be added upon plant λ and then converted to z_{0a} in Klose et al. (2021). All in all, due to insufficient and inadequate observations, all the aforementioned approaches struggle to accurately represent the combined effect of vegetation and rocks on the drag partition and dust emission. In Sect. 3.2, we will propose a novel approach that incorporates both roughness of rocks and plants and equally respects the z_{0a} and λ from both schools of drag partition parameterizations, quantifying the drag partitions of rocks and plants into one hybrid drag partition factor F_{eff}.

Section S3. Description of the Comola et al. (2019) intermittency scheme coupled with Kok et al. (2014b) dust emission equation

In the C19 scheme, the dust emission flux F_d is calculated using the impact threshold (u_{*it}) instead of either the fluid (u_{*ft}) or a combined threshold (u_{*t}). Following the reasoning in Comola et al. (2019b), we update K14 (Eq. 7) with u_{*it} instead of u_{*t} as the threshold (see Sect. 2 for the description of K14 and dust emission thresholds):

$$F_d = C_{tune} C_d f_{bare} f_{clay} \frac{\rho_a (u_{*s}^2 - u_{*it}^2)}{u_{*it}} \left(\frac{u_{*s}}{u_{*it}}\right)^{\frac{C_\alpha (u_{*st} - u_{*st0})}{u_{*st0}}} \qquad \text{for } u_{*s} > u_{*it} \qquad \text{(S3a)}$$

where $u_{*st} = u_{*ft}\sqrt{\rho_a/\rho_{a0}}$ is the same standardized fluid threshold as in the default K14 scheme. Because $u_{*it} < u_{*ft}$, this modified equation accounts for more small dust fluxes that occur due to turbulent winds intermittently driving transport even when $u_* < u_{*ft}$. These fluxes are important over marginal source regions for which emissions are otherwise missed by employing u_{*ft} as the threshold (Comola et al., 2019b).

Next, we account for the intermittency effect on dust emissions by following C19 in introducing the intermittency factor η, which denotes the fraction of time that saltation is active in a model time step (e.g., ~30 mins). η corrects the horizontal sand saltation flux, but since dust emission flux scales with saltation flux (Shao et al., 1993), η is also the fraction of time that dust emission is active in a model timestep. We thus account for the effect of intermittency by multiplying the dust emission flux by η (Comola et al., 2019):

$$F_{d,\eta} = \eta F_d \qquad \text{(S3b)}$$

where $\eta \in [0,1]$.

C19 determines η using the average wind speed, wind fluctuations, and the saltation (and thus dust emission) thresholds. C19 parameterizes η using information at the typical saltation height of $z_{\text{sal}} = 0.1$ m, so we need to first define u_{ft}, u_{it}, and u_s to be u_{*ft}, u_{*it}, and u_{*s} translated to the height of z_{sal} using the log law of the wall:

$$u_X(z_{\text{sal}}) = \frac{u_{*X}}{k} \ln\left(\frac{z_{\text{sal}}}{z_{0a}}\right) \qquad \text{(S4a)}$$

where subscript X could be ft, it or s, $u(z_{\text{sal}})$ is the wind speed at saltation height z_{sal}, z_{0a} is the aeolian roughness length taken here as 10^{-4} m for simplicity (see Martin and Kok, 2018), and k = 0.386 is the von Kármán constant in the atmospheric boundary layer (Andreas et al., 2006). To parameterize the effect of turbulent wind fluctuations on saltation intermittency, we further define $\tilde{u}$ to be the instantaneous wind speed at z_{sal}, which is described by a normal distribution with a mean equal to the model time step mean u and a standard deviation $\sigma_{\tilde{u}_s}$ (Chu et al., 1996), and u_s and $\sigma_{\tilde{u}_s}$ are defined for a time interval of > 10 min. Comola et al. (2019b) then showed that the $\sigma_{\tilde{u}}$ parameterization using the Monin-Obukhov similarity theory (MOST) worked well for in-situ measurements of horizontal saltation fluxes. $\sigma_{\tilde{u}}$ is height invariant and can be parameterized using MOST as (Panofsky et al., 1977):

$$\sigma_{\tilde{u}_s} = u_{*s}\left(12 - 0.5\frac{z_i}{L}\right)^{1/3} \qquad \text{for } 12 - 0.5\frac{z_i}{L} \geq 0 \qquad \text{(S4b)}$$

where L is the Monin-Obukhov length and z_i is the planetary boundary layer (PBL) height. In boundary-layer meteorology, turbulence is generated by mechanical shear and buoyancy (Stull, 1988). The shear-driven turbulence in a flow scales with u_{*s}, while the buoyancy-driven turbulence scales with z_i/L. According to Eq. (S4b), high-frequency wind fluctuations ($\sigma_{\tilde{u}_s}$) increase with shear ($u_{*s} > 0$) and buoyancy ($L < 0$). For larger wind fluctuations $\sigma_{\tilde{u}_s}$, it is easier for $\tilde{u}_s$ to sweep across u_{it} and shut off dust emission, leading to $\eta < 1$. As a result, the emission flux predicted by our scheme will be smaller than the other existing parameterizations for $u_s > u_{ft}$. If $u_s \gg u_{ft}$, $\tilde{u}_s$ will be less likely to sweep across u_{it} and η will approach 1. Furthermore, when $u_{it} < u_s < u_{ft}$, η will be much smaller than one and closer to zero, leading to a small emission flux when other parameterizations predict a zero emission flux. When $u_s < u_{it}$, η could also be greater than zero when $\sigma_{\tilde{u}_s}$ is large enough so that the instantaneous $\tilde{u}_s$ crosses through u_{it}, but the DPM employed would not generate any emission anyway according to Eq. S3a.

With saltation-height variables defined, the total fraction of time η when saltation is active in a model timestep is then formulated as:

$$\eta = 1 - P_{ft} + \alpha(P_{ft} - P_{it}) \tag{S5}$$

where $P_{it} = P(\tilde{u}_s < u_{it})$ is the cumulative probability that the instantaneous wind $\tilde{u}$ does not exceed the impact threshold u_{it}, and $P_{ft} = P(\tilde{u}_s < u_{ft})$ is the cumulative probability that $\tilde{u}_s$ does not exceed the fluid threshold u_{ft}. The fluid threshold crossing fraction α is defined as the fluid threshold crossing rate C_{ft}, which is the number of times $\tilde{u}_s$ sweeps across u_{ft} per second, divided by the total crossing rate $C_{ft} + C_{it}$, which is the number of times $\tilde{u}_s$ sweeps across u_{ft} and u_{it} per second: $\alpha = \frac{C_{ft}}{C_{ft}+C_{it}}$. α approaches 1 when instantaneous wind $\tilde{u}_s$ mostly crosses u_{ft}, and approaches 0 when $\tilde{u}$ mostly crosses u_{it}. C19 showed that α is a function of u_s, $\sigma_{\tilde{u}}$, u_{it}, and u_{ft}:

$$\alpha \approx \left[\exp\left(\frac{u_{ft}^2 - u_{it}^2 - 2u_s(u_{ft} - u_{it})}{2\sigma_{\tilde{u}_s}^2}\right) + 1\right]^{-1} \tag{S6a}$$

such that $\alpha \rightarrow 1$ in the limit of $u_s \gg u_{ft}$, and $\alpha \rightarrow 0$ for $u_s \rightarrow 0$ and $\sigma_{\tilde{u}_s} \rightarrow 0$. As for P_{ft} and P_{it}, assuming a Gaussian distribution for $\tilde{u}$, i.e., $\tilde{u}_s \sim \mathcal{N}(u_s, \sigma_{\tilde{u}_s}^2)$, P_{ft} and P_{it} can be expressed using the error functions $\mathrm{erf}(x)$ as:

$$P_{ft} = \frac{1}{2}\left[1 + \mathrm{erf}\left(\frac{u_{ft} - u_s}{\sqrt{2}\sigma_{\tilde{u}_s}}\right)\right] \tag{S6b}$$

$$P_{it} = \frac{1}{2}\left[1 + \mathrm{erf}\left(\frac{u_{it} - u_s}{\sqrt{2}\sigma_{\tilde{u}_s}}\right)\right] \tag{S6c}$$

Within a model timestep, dust emission is continuous for the fraction of time $1 - P_{ft}$ when $\tilde{u}_s > u_{ft}$, and for the fraction of time $P_{ft} - P_{it}$ dust emission is in the hysteresis regime ($u_{it} < \tilde{u}_s < u_{ft}$) where dust emission can only be active for a fraction of time α when $\tilde{u}_s$ crossed u_{ft} more recently than u_{it} in the hysteresis regime. Using Eqs. S3–S6, we computed η from Eq. S3b, yielding the dust emission flux $F_{d,\eta}$ that accounts for the effects of intermittency.

We note that the C19 scheme is designed for GCMs and RCMs in RANS mode (not in LES mode), regardless of the time step used.

Section S4. Calculating the Obukhov length L from MERRA-2 meteorological fields

MERRA-2 does not include the Obukhov length L, but outputs several variables that allows us to compute L, using (Bonan, 2015; Lee and Buban, 2020):

$$L = -\rho_a c_p T u_*^3 / kgH, \tag{S7}$$

where ρ_a is air density (kg m^{-3}), c_p is the specific heat capacity of air under constant pressure (J kg^{-1} K^{-1}), T is air temperature (in this study we chose T_{10}, which is air temperature at the height of 10 m), u_* is friction velocity (m s^{-1}), k is the von Kármán constant, g is gravitational acceleration (m s^{-2}), and H is the sensible heat flux (W m^{-2}). MERRA-2 provides sensible heat flux (SHLAND) and T_{10} (T10M), allowing us to directly compute L.

Section S5. Comparing our simulated dust emission threshold against observationally derived Pu et al. (2020) threshold

Here we make a comparison between our simulations of dust emission thresholds and the observationally based threshold estimate from Pu et al. (2020). They compared the wind speed distributions from reanalyses against observationally derived DAOD distributions to obtain a threshold wind speed $u_{t,Pu}$ for each gridbox (Fig. S13 below) that corresponds to a threshold DAOD value (i.e., 0.5 over arid regions and 0.05 over semiarid regions), above which is defined as a dust emission event.

In this paper, we argue that dust emission equations should employ the impact threshold u_{*it}. Given that $u_{t,Pu}$ was obtained by matching DAOD distributions against the distributions of wind speed u, $u_{t,Pu}$ is more relevant to the impact threshold u_{it} than the fluid threshold u_{ft} (i.e., the moisture effect is less relevant). Furthermore, Pu et al. (2020) used wind speed u at 10 m instead of the soil surface wind speed u_s $(= uF_{eff})$ in the analysis, and thus $u_{t,Pu}$ captured a larger threshold wind speed that included the impact threshold u_{it} as well as the drag partition effect F_{eff} that inhibits saltation. To make a fair comparison, we compare here $u_{t,Pu}$ against our u_{*it} divided by the drag partition factor, u_{*it}/F_{eff}, which is larger than u_{*it}. We used the log law of the wall (Eq. S4a) to change u_{*it} from a velocity scale to a velocity of u_{it} at the level of z = 10 m, yielding u_{it}/F_{eff} instead.

In Fig. S13, the top two panels show the Pu et al. (2020) annual mean threshold $u_{t,Pu}$ (Fig. S13a) and the u_{it}/F_{eff} from our scheme (Fig. S13b). Both maps share similar spatial variability and magnitudes over certain regions such as Africa and Australia. The bottom panels show the bias (Fig. S13c) and ratio (Fig. S13d) of the thresholds, showing that the larger discrepancies occur over East and Central Asia. For instance, over the Kyzylkum, $u_{t,Pu}$ is 4–7 m s^{-1} higher than our threshold. In general, Fig. S13c shows that, over most emission source regions, $u_{t,Pu}$ and our threshold are relatively close to each other and differ by ~1–2 m s^{-1}. This comparison shows that both methods derived dust emission thresholds of similar magnitudes and moderate spatial consistency.

We note two small caveats to this comparison. First, $u_{t,Pu}$ was derived by using a DAOD threshold as a proxy for defining an emission event, such that the inferred threshold depends on the extent to which non-local dust is advected from upwind regions instead of emitted locally. This transport effect might cause a lower $u_{t,Pu}$ in downwind regions, such as over the Sahel, as seen in Fig. S13a. Therefore, the global spatial pattern of $u_{t,Pu}$ partially reflects the DAOD spatial variability. Second, our u_{it}/F_{eff} (Fig.13b) is an annual mean, including those high-LAI seasons when there are no dust emissions. Therefore, removing seasons with high LAI and low emissions would likely yield a smaller mean u_{it}/F_{eff} over semiarid regions, which might better represent the annual threshold wind speed (beyond which dust emission occurs).

Section S6. A detailed discussion of the caveats and limitations of the new dust emission scheme

6.1. Soil median diameter representation

For our derived parameterization for the dry soil median diameter $\overline{D}_p$, we obtained a relationship between $\overline{D}_p$ and silt+clay fraction for non-arid regions (LAI > 1), and a constant of $\overline{D}_{p0} = 127 \pm 47$ μm for arid regions (LAI < 1). In theory, $\overline{D}_p$ should be a function of soil properties (Hillel, 1980) and therefore implicitly of space and time, but we obtained a simple relationship for $\overline{D}_p$ over arid regions because 1) different studies provided measurements of different soil properties such that data are limited and insufficient for a more detailed statistical analysis, 2) the uncertainties of the measured soil PSDs are moderately large, and 3) most $\overline{D}_p$ measurements over arid regions found $\overline{D}_p$ within 40–250 μm (Fig. 1c), which limited the dry fluid threshold u_{*ft0} to vary within the relatively small range of ~0.204–0.268 m s^{-1} (from Eq. 2 assuming $\rho_a = 1.225\ \mathrm{kg\ m^{-3}}$). This range is about ten times smaller than the global range of the wet fluid threshold u_{*ft} (~ 1 m s^{-1}). Thus, using a single $\overline{D}_{p0} \sim 127$ μm across all arid regions appears to be a reasonable approach given the current data availability.

A number of previous studies have also compiled their global $\overline{D}_p$ maps for calculating the dust emission threshold (Laurent et al., 2008; Tegen et al., 2002; Menut et al., 2013). These studies used global soil texture data (with known fractions f_a of soil components including sand, silt, and clay) to determine gridded soil types using the soil texture triangle diagram (e.g., FAO/IIASA/ISRIC/ISS–CAS/JRC, 2012; Chatenet et al., 1996; Shirazi and Boersma, 1984), and calculated gridded $\overline{D}_p$ maps by combining the soil component fractions f_a with the estimated aggregated particle size $\overline{D}_a$ of the soil components by a weighted mean $\overline{D}_p = \sum_a f_a \overline{D}_a$ (Menut et al., 2013). Since these $\overline{D}_a$ values are based on measurements from Chatenet et al. (1996), these studies also took into account the aggregated sizes of the individual soil components. However, owing to insufficient data worldwide, these maps have not been verified against the measurements of the in-situ soil PSD. On the other hand, our results based on observations suggest that the spatial variability of $\overline{D}_p$ over deserts are relatively small compared to $\overline{D}_p$ over nonarid regions, and does not significantly correlate with soil texture and soil properties (see Eq. 14). Our results thus surprisingly suggest that the $\overline{D}_p$ parameterization can reasonably be much simplified into a global constant over arid regions. This approach is consistent with another current approach of employing a globally constant soil particle diameter (e.g., Zender et al., 2003a; Mahowald et al., 2006) and significantly different from another approach of employing a $\overline{D}_p$ map (e.g., see Fig. S10 for the input $\overline{\mathrm{D}}_\mathrm{p}$ map for the CHIMERE CTM; Mailler et al., 2017; Menut, 2018; Menut et al., 2021). Furthermore, the $\overline{D}_p$ measurements showed a positive relationship with the silt+clay fraction $f_{silt+clay}$ over the non-arid regions, which we attributed to the increasing cohesion between soil particles with the increasing silt+clay content. This is different from the negative $\overline{D}_p$–$f_{silt+clay}$ relationship assumed by most past studies (Tegen et al., 2002; Laurent et al., 2008; Menut et al., 2013) as they assumed that $\overline{D}_p$ increased with sand content ($f_{sand} = 1 - f_{silt+clay}$). We argue that our $\overline{D}_p - f_{silt+clay}$ relationships are based on observations and should thus represent an improvement over the past assumed $\overline{D}_p$–texture relationships. We anticipate that as more measurements emerge in the future, more statistical or machine learning modeling approaches can more robustly decipher the intricate relationships between the aggregated $\overline{D}_p$ and the soil properties in order to further improve the representation of the global $\overline{D}_p$ map.

6.2. Hybrid drag partition scheme

For our drag partition scheme, we combined the drag partition for rocks ($f_{eff,r}$) from the Marticorena and Bergametti (1995) scheme with the drag partition for vegetation ($f_{eff,v}$) from the Okin (2008) scheme using a weighted mean approach employing the land cover fractions of rocks and vegetation, which is a novel approach. Nonetheless, our scheme still contains several major limitations. First and foremost, we calculate the rock $f_{eff,r}$ using the Prigent et al. (2005) aeolian roughness length data derived from the ERS microwave sensor, but we could not completely separate rock roughness from vegetation roughness in the dataset. Marticorena et al. (2006) argued that ERS sensor measurements has relative small local incident angles such that the contribution from vegetation roughness is relatively small compared to the contribution from rock roughness. We also removed as much vegetation influence as possible on z_{0a} by taking the minimum z_{0a} out of the 12 available monthly data for all grids, but it is still possible that a small fraction of vegetation roughness remains. Thus, our approach of combining the time-invariant Pr05 z_{0a} (and $f_{eff,r}$) with the time-varying $f_{eff,v}$ will probably result in a small degree of double-counting of vegetation roughness in our drag partition scheme. We also note that the Pr05 data used the microwave backscatter coefficient as a proxy for inferring z_{0a}, but it does not perfectly correlate with the z_{0a} measured by the ground sites, and so there will be some corresponding errors in the Pr05 z_{0a} used in our drag partition scheme.

Second, the land cover fraction areas used are obtained from the ESA CCI dataset in our drag partition scheme, which are annual mean and thus not season-dependent. The land cover of vegetation A_v in Eq. 21b should also be a function of time mainly because of the seasonally changing vegetation cover. However, most current land cover datasets provide annual data but not seasonal data, and thus A_r and A_v in Eq. 21b are only spatially varying within the year 2006. Furthermore, most land cover datasets only provide near-term land cover data (the farthest data goes back to the year 850; e.g., Klein Goldewijk et al., 2017). ESA CCI has a temporal coverage of 1992–2019, and so the dataset will represent relatively well for present-day scenarios but become less representative of paleoclimatological scenarios, for which the vegetation distributions differ from that in the present day, such as during the Green Sahara > 6000 years ago (Kutzbach et al., 1996; Bonan, 2015).

A third limitation of our new drag partition scheme is that the Okin (2008) drag partition scheme requires the vegetation cover fraction f_v as a proxy for vegetation density. In this study, we proposed LAI ~ $f_v = 1 - f_{bare}$ as discussed in Eq. 18b. Since LSMs do not have accurate simulations of f_v, there are only preliminary equations for calculating the bare and vegetated fractions proposed by previous papers (e.g., Mahowald et al., 2006; see discussions in Eq. 11 and Eq. 18b). However, Eq. 11 (and thus f_v ~ LAI) only applies to regions with low LAI because leaves are mostly not overlapped; over regions with higher LAI, leaves start to overlap and LAI > f_v. Thus, this assumption could overestimate f_v and thus $f_{eff,v}$, thereby underestimating dust emissions over vegetated regions (e.g., underestimations over western U.S. deserts in Fig. 7e). Thus, LSMs need a more accurate parameterization of f_v to get a more accurate vegetation drag partition effect regardless of whether the Okin (2008) or the Raupach et al. (1993) scheme is used. Alternatively, LSMs could also read in observed f_v from available satellite-derived products such as MODIS or AVHRR f_v, as done by Wu et al. (2016) for instance. We used the observed/modeled LAI instead of observed f_v, because LSMs actively simulate LAI, allowing the scheme to be used in past and future climates when vegetation cover observations are not available.

A fourth important limitation is that O08 does not fundamentally distinguish the drag partitioning between different plant functional types (PFTs). O08 assumes that all short plants are hemispheric in shape and produce the same $f_{eff,v}$ if they have the same f_v or LAI. In reality, short plants such as shrubs, herbaceous plants, and crops have vastly different shapes; some are far from hemispheric and can hardly be approximated by a simple geometry or shape. Nonetheless, this limitation is not unique to O08 but shared by other drag partition schemes such as Raupach et al. (1993), as their $f_{eff,v}$ equations are also functions of f_v only and not functions of PFTs. More research is thus warranted in the future to better quantify the plant shapes and $f_{eff,v}$ of different PFTs.

6.3. Dust emission intermittency scheme

There are two important caveats about the Comola et al. (2019b) intermittency scheme. The first caveat is that it has exponential dependences on u_{*s}, $\sigma_{\tilde{u}_s}$, u_{*it}, and u_{*ft} (see Sect. S3) and is thus very sensitive and vulnerable to the accuracy of the GCM simulations of the four variables. For instance, if the thresholds are overestimated by the threshold schemes, not only will emissions be underestimated but η from C19 will also be close to zero and further worsen the low bias of the dust emissions. Therefore, a prerequisite of employing the C19 scheme is that the wind u_{*s} and the thresholds should be adequately simulated and have reasonable ranges of variability throughout the year. If simulated well, η will have reasonable day-to-day and seasonal fluctuations. Otherwise, η can constantly fall on one or zero and become unindicative of the boundary-layer dynamics temporal variability, and the resulting η time series will further impact and worsen the temporal variability of the $F_{d,\eta}$ time series.

There is a second caveat about a technical flaw in C19. When $u_{*s} < u_{*it}$ in a time step, while Comola's theory allows turbulence to generate instantaneous winds $\tilde{u}_s$ that exceed the impact and fluid thresholds and generate some emissions (even when the averaged $u_{*s} < u_{*it}$ across the model timestep), the setup in Eq. S3 by nature could not allow emissions when $u_{*s} < u_{*it}$. C19 allows $\eta > 0$ (per Eq. S5) when $u_{*s} < u_{*it}$. However, the way C19 was parameterized was such that C19 still depends on conventional dust emission equations such as Kok et al. (2014b) or Zender et al. (2003a), which by nature prohibit emissions when the mean $u_{*s} < u_{*it}$ within a model time step (Eq. S3). This means that the C19 theory and the C19 dust emission parameterization contain an internal logical inconsistency, and the C19 scheme per se still does not generate emissions $F_{d,\eta}$ (Eq. S3b) for $u_{*s} < u_{*it}$ ($\eta > 0$ per Eq. S5, but $F_{d,\eta} = \eta F_d = 0$ since $F_d = 0$ per Eq. S3). But, because the turbulent emissions in the $u_{*s} < u_{*it}$ regime is small, the C19 formulation is still a good approximation for turbulent emissions, performing much better than the conventional timestep-constant models as demonstrated in Comola et al. (2019b).

6.4 Reducing the grid scale-dependence of dust emission simulations

We produced the correction maps to scale the spatial variability of the low-resolution dust emission simulations, matching the spatial variability of the high-resolution emissions (Fig. 9) to reduce the scale-dependence of dust emission simulations. As such, it is an alternative to the computationally expensive but more fundamental solution of simulating dust emissions in the highest model resolution possible and then regrid to coarser resolution. Employing the scaling map $\widetilde{K}_c$ is different from the fundamental solution in the sense that the maps in Fig. 9 are time-independent and derived by matching the annual total high-resolution emissions (Sect. 4.2). As seen in Fig. S10, the scaling map exhibits a moderate degree of seasonality, but employing an annual scaling map like Fig. 9 will already address a large part of the scale-dependence problem. We suggest GCMs and CTMs, which focus on present-day simulations, perform multiyear simulations in both high and native grid resolutions to obtain monthly climatological maps of scaling factors for present-day dust emission simulations. Afterwards, ESMs only need to read in the climatological monthly scaling maps to rescale the native grid dust emissions every month before passing the dust emissions to the atmospheric model component. If desired, instead of generating climatological maps, models can even choose to obtain transient (e.g., monthly) $\widetilde{K}_c$ maps as a time series for the past decades of the historical period (e.g., 1980–2020) so that the scaling maps contain a much better temporal variability in terms of seasonality, interannual and decadal variability, of the historical dust emissions than compared with the climatological scaling maps.

Our proposed approach is an alternative to a more common approach, which is to employ a Weibull distribution to the GCM winds (Cakmur et al., 2004; Grini et al., 2005; Cowie et al., 2015; Zhang et al., 2016; Menut, 2018; Tai et al., 2021). In the Weibull approach, in each time step the model assumes a Weibull PDF for each grid that is characterized by the modeled mean wind speed and a shape parameter k representing the subgrid wind variability. k could be a global constant (e.g., k = 4 in Menut, 2018), a parameterized function of the model mean wind speed (e.g., Grini et al., 2005), or a globally gridded map obtained by comparing coarse winds against high-resolution winds (Ridley et al., 2013; Tai et al., 2021). A distinction between our approach and the Weibull approach is that while previous studies derived the shape parameter by comparing high- and low-resolution winds (e.g., Tai et al., 2021), we directly make use of the high- and low-resolution input fields to calculate dust emissions (Figs. 8c and d) and then compare between the high- and low-resolution emissions. Therefore, the correction map $\widetilde{K}_c$ (Fig. 9) captures subgrid wind variability due to subgrid spatial characteristics just like k in the Weibull approach, and thus we anticipate some intrinsic spatial correlations between the $\widetilde{K}_c$ and k maps.

However, there are three distinctions and advantages of our approach over the Weibull approach. The first and the most important one is that our approach accounts for not only the subgrid variability of wind but all other fields (u_{*s}, w, LAI, etc). $\widetilde{K}_c$ is obtained via comparing emissions across resolutions and thus its magnitude is a result of the subgrid variability of all input fields, whereas in Tai et al. (2021) the k is obtained via comparing winds across resolutions and thus only captures subgrid wind variability. The second advantage is that our approach makes no assumption about the distributions of the subgrid variability of forcings. The Weibull approach is a parametric statistical method, which means the dust models need to assume the subgrid winds follow a Weibull distribution, but the subgrid spatial wind variability can deviate substantially from a Weibull distribution due to several reasons, such as complex terrain (Jiménez et al., 2011). Our method is non-parametric and thus more robust in capturing subgrid variability of multiple input fields at once. The third advantage is that our approach saves computational cost because it only needs to (1) find the $\widetilde{K}_c$ map and (2) directly apply $\widetilde{K}_c$ to correct the coarse emissions. Meanwhile, past studies needed to (1) find the k map, (2) iteratively calculate emissions by looping across the Weibull PDF (3) sum across the PDF to yield the total emission, and (4) update the Weibull PDF for each grid and time step. Repeating step (2) for all times and grids is computationally very expensive.

There is yet another alternative approach to account for subgrid variability of winds and other parameters. Some CTM studies (e.g., Meng et al., 2021) proposed to simulate dust emissions at the highest resolution possible and then store the results as a gridded emission inventory. Meng et al. (2021) proposed that CTMs do not need to simulate dust emissions and instead only need to regrid the stored gridded dust emissions to the desired grid resolutions. An advantage of their approach is clearly that their regridded dust emissions will have the correct spatial and temporal correlations with their high-resolution dust emission inventory, which means there will be no grid scale-dependence problem in their approach. Their approach also saves time and computational resources because they do not simulate but just read in and regrid dust emissions. This approach is particularly favorable for the CTM simulations for air quality forecasts and hindcasts in which models need to ensure the near-term input meteorological fields are very accurate to generate an accurate dust emission inventory, such as the air quality forecasts conducted by the Environmental Protection Agency (EPA) using CMAQ (Appel et al., 2013, 2017), or other CTM studies such as GEOS-Chem (Zhang et al., 2013; Meng et al., 2021). However, for GCMs/ESMs that care about long-term simulations and aerosol–climate interactions, there is a need to actively simulate dust emissions and allow a full coupling between meteorology and dust, which could not be achieved by feeding the models with an inventory. In that case, our scaling method is likely more desirable for GCMs and ESMs to reduce the scale-dependence problem.

Also, we note that although our approach alleviated the grid-scale dependence of dust emissions, the grid-scale dependence problem also appears in other component of dust cycle simulations, such as in dust transport. The grid-scale dependence can be due to not just the averaging problem but also other problems, such as numerical diffusion which worsens with increasing grid size in an Eulerian GCM (Rastigejev et al., 2010; Eastham and Jacob, 2017; Zhuang et al., 2018). It has to be solved in the atmospheric model component such as by some adaptive mesh refinement approaches (e.g., Semakin and Rastigejev, 2016) or machine learning methods (e.g., Zhuang et al., 2021).

Table S1. Past studies employed in this paper that collected dry soil aggregate size distributions over different countries.

Study	Number of samples we used	Location of the sites	Aridity[a]
Ciric et al. (2012)	5	Pannonian Basin, Serbia	nonarid
Li et al. (2014)	4	Tarim Basin	arid
Wagner et al. (1992)	2	Kansas	arid
Chandler et al. (2004)	3	Columbia Plateau	arid
Mei et al. (2004)	4	Northern China	arid
Swet and Katra (2016)	2	Negev, Israel	arid
Mirzamostafa et al. (1998)	2	Kansas	nonarid
Liu et al. (1998)	3	Inner Mongolian Plateau &Tengger Desert, China	arid
Kalhoro et al. (2017)	6	Loess Plateau	nonarid
Su et al. (2007)	4	Hexi Corridor	arid
Udom and Ogunwole (2015)	4	Port Harcourt, Nigeria	nonarid
Malobane et al. (2019)	2	University of Fort Hare	nonarid
Klose et al. (2017)	5	New Mexico	arid
Shao et al. (2011)	1	Victoria, Austrialia	arid

[a]The aridity of the sampling site was classified by this study based on whether the annual mean MERRA-2 LAI (see Fig. 3a in the main text) is smaller or larger than 1.

Table S2. The global total redistributions in the normalized emissions from each modification.

	Using $\overline{D}_p$ = 127 μm[a]	Including F_{eff}[b]	Including the intermittency[c]	Our scheme compared with K14[d]
Arid	216 Tg yr^{-1}	3257 Tg yr^{-1}	3075 Tg yr^{-1}	3663 Tg yr^{-1}
Nonarid	34 Tg yr^{-1}	354 Tg yr^{-1}	87 Tg yr^{-1}	395 Tg yr^{-1}
Globe	250 Tg yr^{-1}	3611 Tg yr^{-1}	3163 Tg yr^{-1}	4058 Tg yr^{-1}

[a]Normalized Expt. II minus normalized Expt. I (Fig. S7a).
[b]Normalized Expt. III minus normalized Expt. II (Fig. S7b).
[c]Normalized Expt. V minus normalized Expt. III (Fig. S7e).
[d]Normalized Expt. V minus normalized Expt. I (Fig. S7f).

Table S3. The global total emissions all simulations schemes and their contributions from arid and nonarid regions.

	Original emissions	Normalized emissions	% of emissions from arid regions	% of emissions of nonarid regions
K14	29254 Tg yr^{-1}	5000 Tg yr^{-1}	92.1 %	7.9 %
Our scheme	11494 Tg yr^{-1}	5000 Tg yr^{-1}	97.8 %	2.2 %
MERRA-2	1561 Tg yr^{-1}	5000 Tg yr^{-1}	97.3 %	2.7 %
Z03–Z	424 Tg yr^{-1}	5000 Tg yr^{-1}	100 %	0 %
Z03–G	442 Tg yr^{-1}	5000 Tg yr^{-1}	100 %	0 %

Table S4. Regional contributions of dust emissions to the global total emission for different schemes. [a, b]

	DustCOMM & B16[c]	K14	Our scheme	Z03–Z	Z03–G	MERRA-2
NW Africa	18 %	10.4 %	14.4 %	7.5 %	23.2 %	20.1 %
NE Africa	16 %	17.5 %	14.5 %	13.3 %	17.9 %	17.1 %
Sahel	13 %	17.4 %	15.9 %	20.8 %	16.5 %	21.5 %
Middle East / C Asia	29 %	29.4 %	30.6 %	32.5 %	31.3 %	29.2 %
E Asia	13 %	4.1 %	11.9 %	14.3 %	4.0 %	6.5 %
N America	3 %	1.8 %	1.1 %	0.1 %	0.02 %	0.5 %
Australia	3 %	10.8 %	6.4 %	9.7 %	6.8 %	2.6 %
S America	4 %	2.3 %	2.2 %	0.5 %	0.07 %	1.7 %
S Africa	2 %	6.3 %	3.0 %	1.4 %	0.3 %	0.7 %
high-lat (w/ Patagonia)	5 % (from B16)	2.8 %	6.3 %	0.2 %	0.2 %	1.7 %

[a]All percentages from MERRA-2 and our simulations are rounded to 1 decimal place, except for smaller values where we rounded to 2 decimal places.

[b]Bullard et al. (2016) obtained 5 % including Patagonia emissions, which overlaps with the S. America domain defined in Kok et al. (2021a, b). We present the percentage here assuming the nine K21 source regions sum up to be 100 %, since K21 (DustCOMM) predicted zero emissions outside of the domains (including B16 will yield 105 %). We arrange the other columns the same way such that the percentages from the nine K21 regions sum up to 100 % also.

[c]Values are directly obtained from Table 2 of Kok et al. (2021b), which were rounded up to integers, except for high-latitude emissions that are obtained from Bullard et al. (2016).

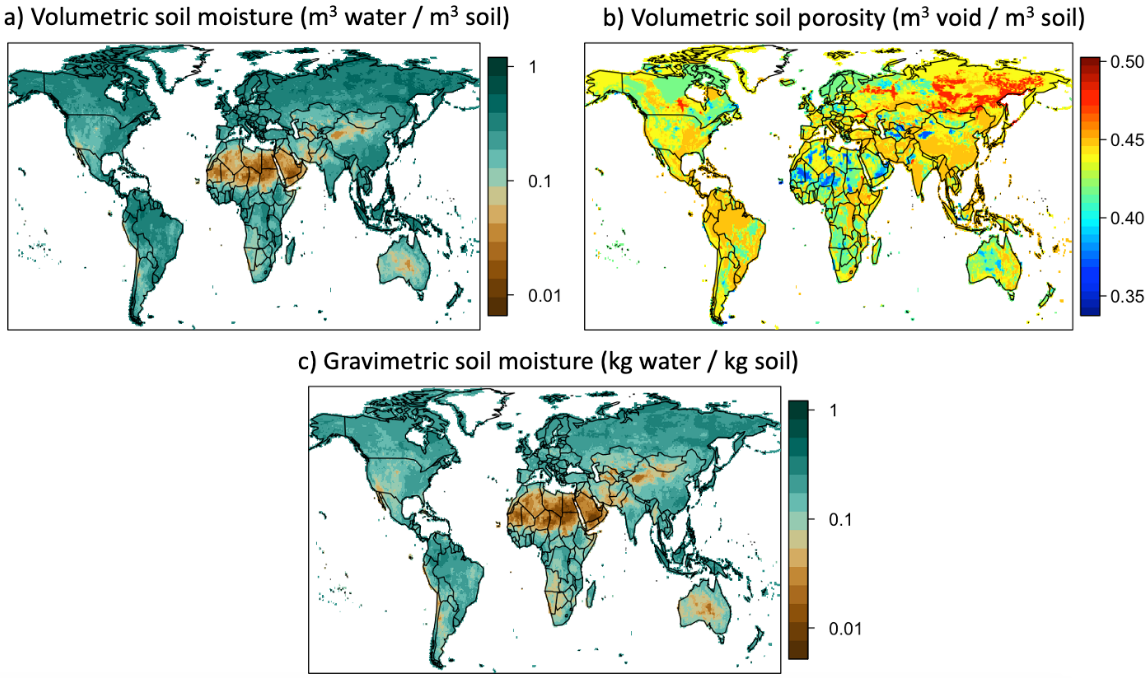

Figure S1. MERRA-2 soil moisture for the year 2006 used in this study. (a) Volumetric soil moisture (m^3 m^{-3}), (b) soil porosity, and (c) gravimetric soil moisture (kg kg^{-1}).

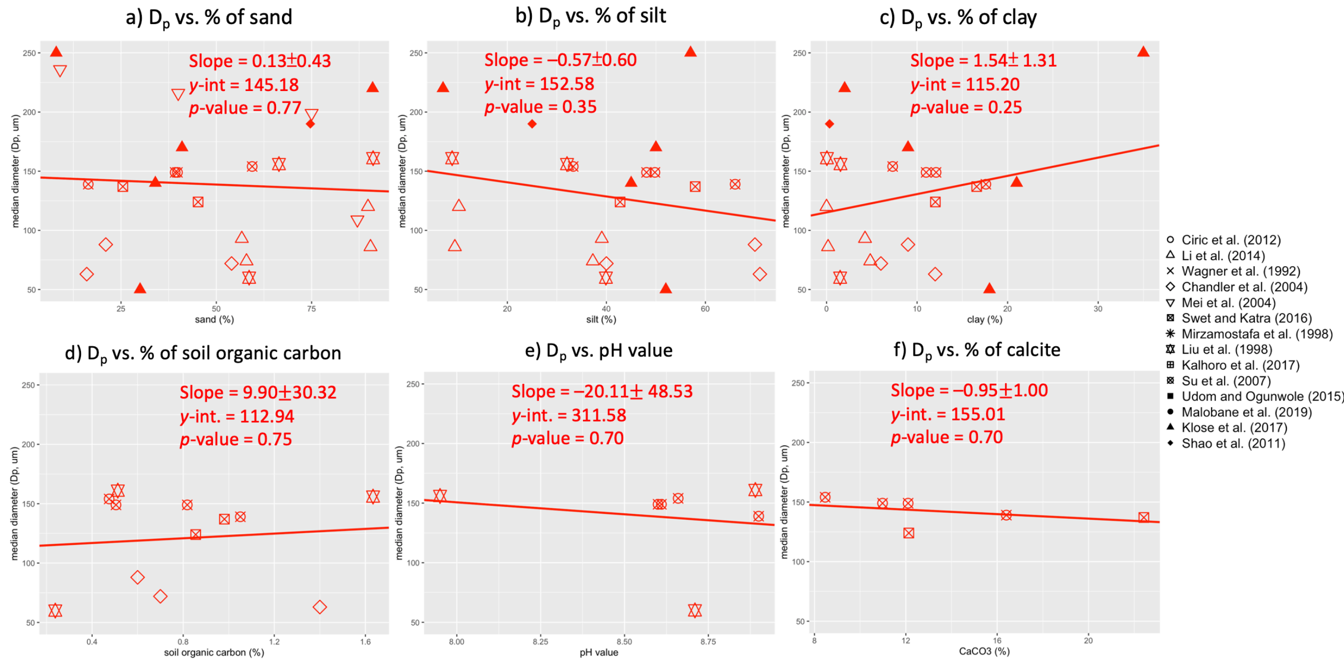

Figure S2. The relationships between soil median diameter $\overline{D}_p$ and soil texture and other soil properties documented in multiple past studies for arid regions. We relate D_p to content of (a) sand, (b) silt, (c) clay in %, as well as to (d) soil organic carbon (SOC) content in %, (e) pH value, and (f) % of calcite ($CaCO_3$). The symbols show the name of each individual study and lines denote linear regressions for which statistics are included for each panel. Studies may not have documented certain texture or properties, so some plots have fewer data points (especially for soil properties).

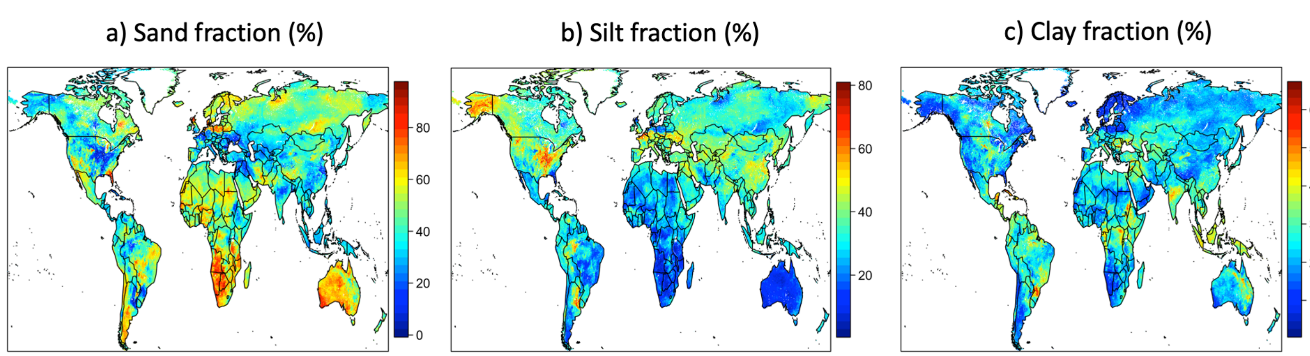

Figure S3. The SoilGrids global 0.1° × 0.1° maps of (a) sand, (b) silt, and (c) clay in % (Hengl et al., 2017).

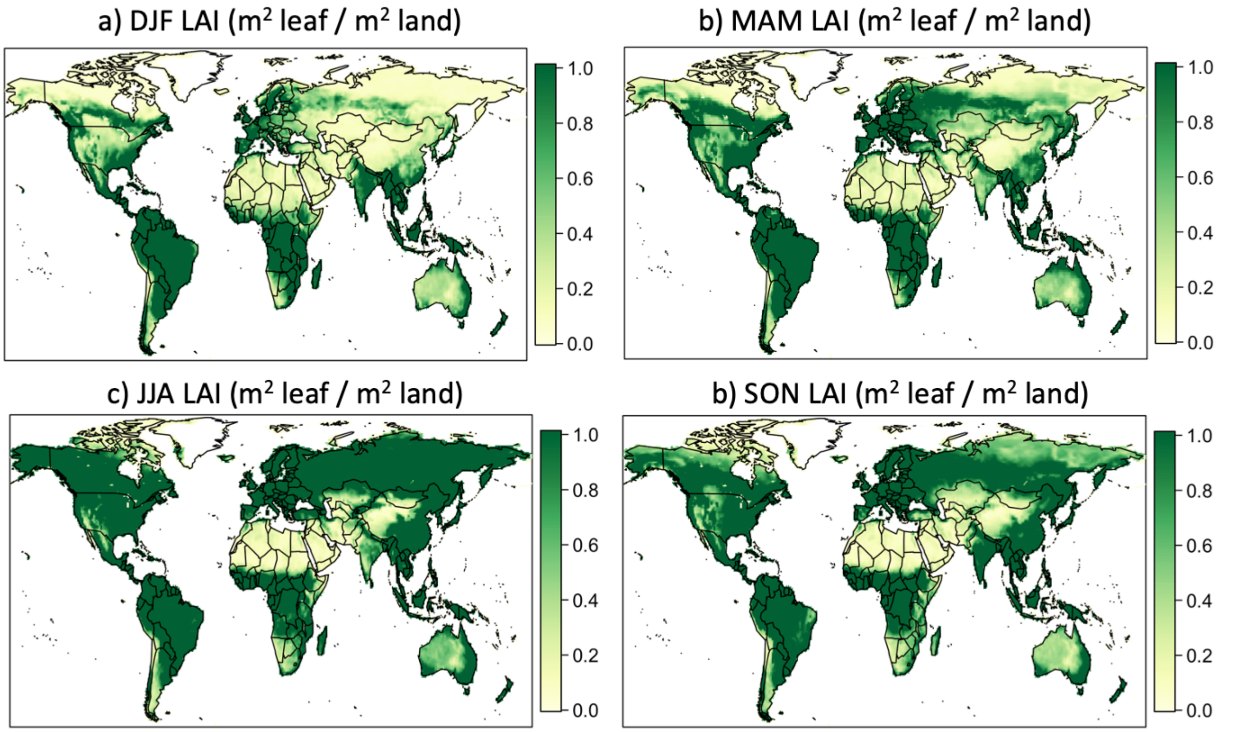

Figure S4. Global distributions of MERRA-2 seasonal mean LAI for the year 2006. Four seasonal mean LAI maps are plotted, including the (a) December–January–February, (b) March–April–May, (c) June–July–August, and (d) September–October–November. The color bar saturates at 1, so regions in dark green color have LAI > 1 and are defined as non-arid area in this study.

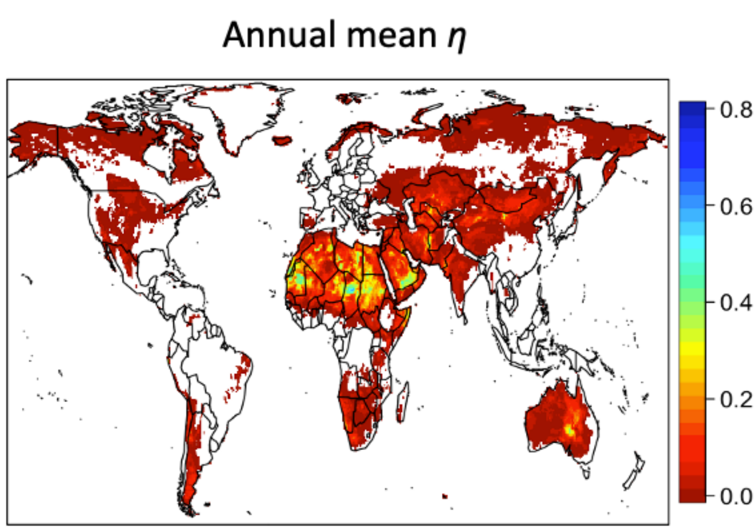

Figure S5. The annual mean intermittency factor η, which denotes the fraction of time within a time step that emission is active, averaged over the whole year 2006.

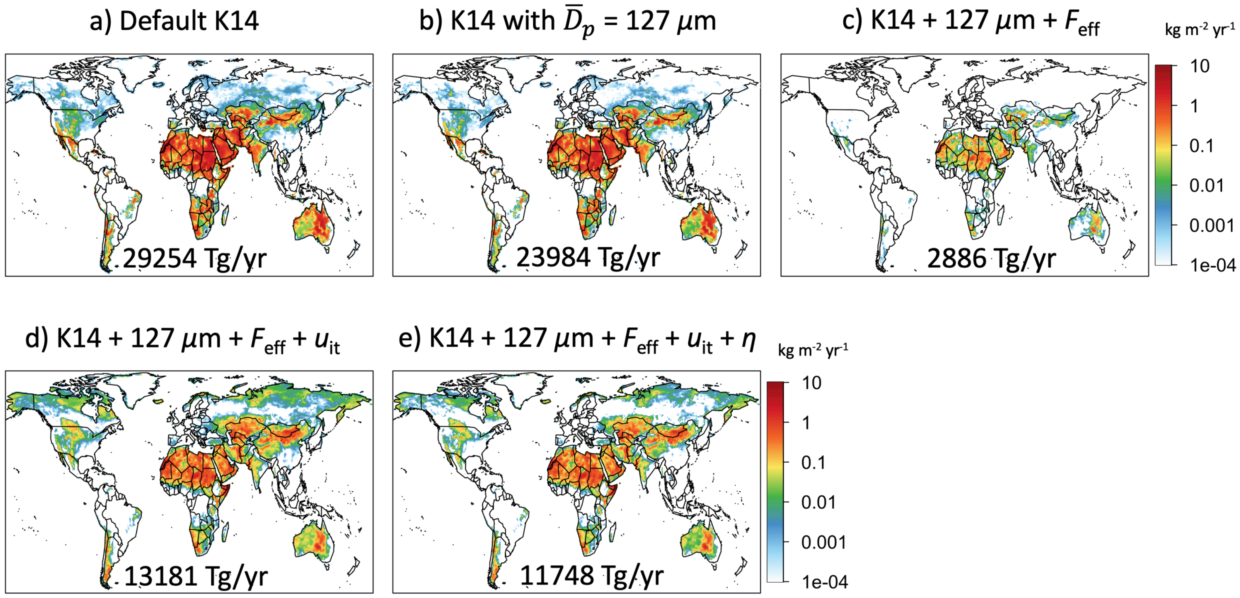

Figure S6. Spatial patterns of the unnormalized dust emission flux for each modification of the default dust emission scheme. The plots include results for the (a) default K14 scheme (expt. I), (b) K14 with changed soil particle diameter only (expt. II), (c) K14 with the new soil particle diameter and drag partition effect (expt. III), (d) K14 with the new soil particle diameter, drag partition effect, and impact threshold (expt. IV), and (e) K14 with all modifications, i.e., our new scheme (expt. V). The bottom of each panel notes the unnormalized global total emission in Tg yr^{-1}.

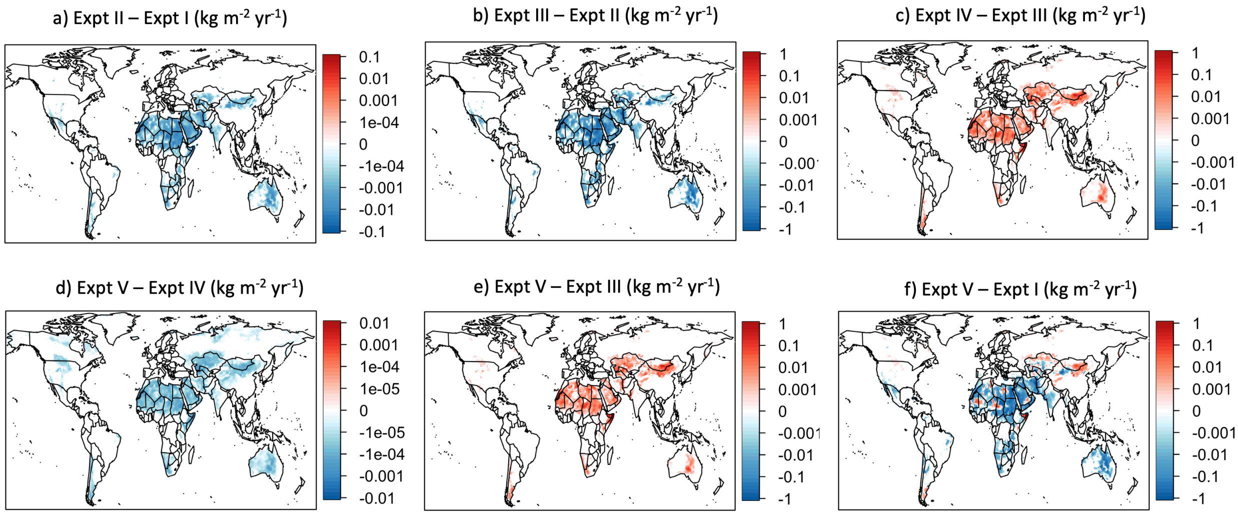

Figure S7. The effects of the proposed improvements to the parameterization of dust emissions on the default (Kok et al., 2014a, b) dust emission scheme. Maps of unnormalized emission differences with individual improvements added on top of the default K14 scheme. The individual improvements are respectively (a) changing the soil median diameter to 127 μm (expt. II), (b) including the drag partition effect (expt. III), (c) employing the impact threshold, (d) applying the intermittency factor, and (e) including the Comola et al. (2019b) intermittency scheme, a combination of (c, d). (f) Maps of unnormalized emission differences between our new scheme and the K14 scheme. The color bars of the maps of differences are drawn to $\log_{10}$ scale.

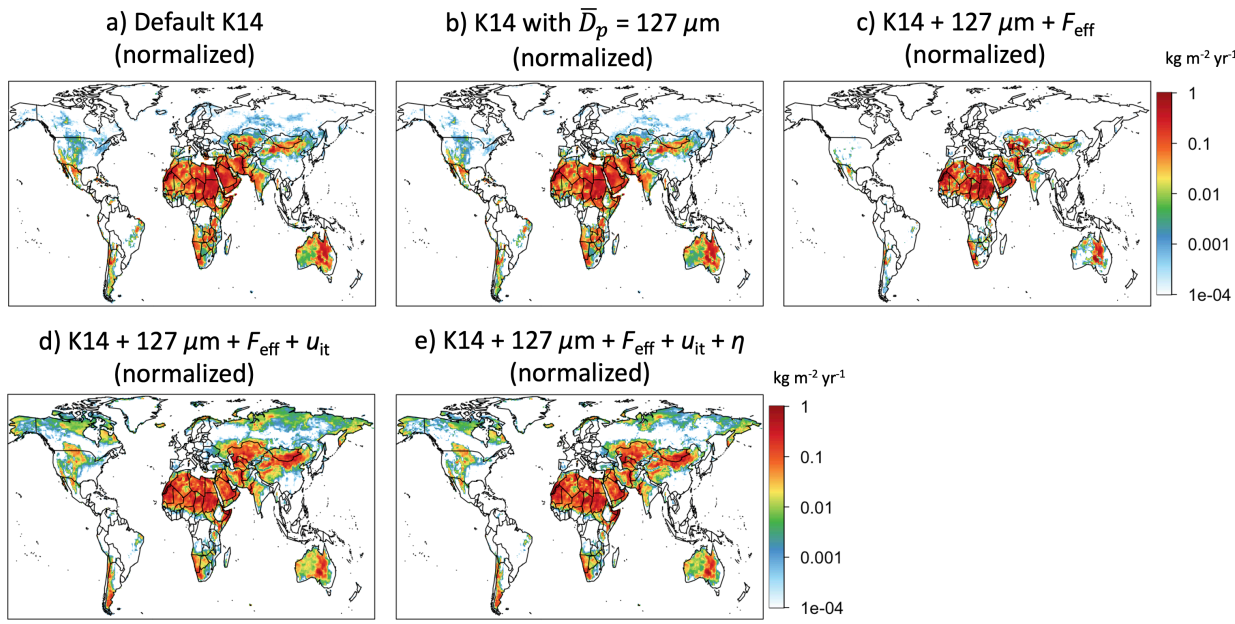

Figure S8. Spatial patterns of the normalized dust emission flux for each modification of the default dust emission scheme (same as Figure S6 but normalized). The plots include results for the (a) default K14 scheme (expt. I), (b) K14 with changed soil particle diameter only (expt. II), (c) K14 with the new soil particle diameter and drag partition effect (expt. III), (d) K14 with the new soil particle diameter, drag partition effect, and impact threshold (expt. IV), and (e) K14 with all modifications, i.e., our new scheme (expt. V). All plots are normalized to have a global total emission of 5000 Tg yr^{-1}.

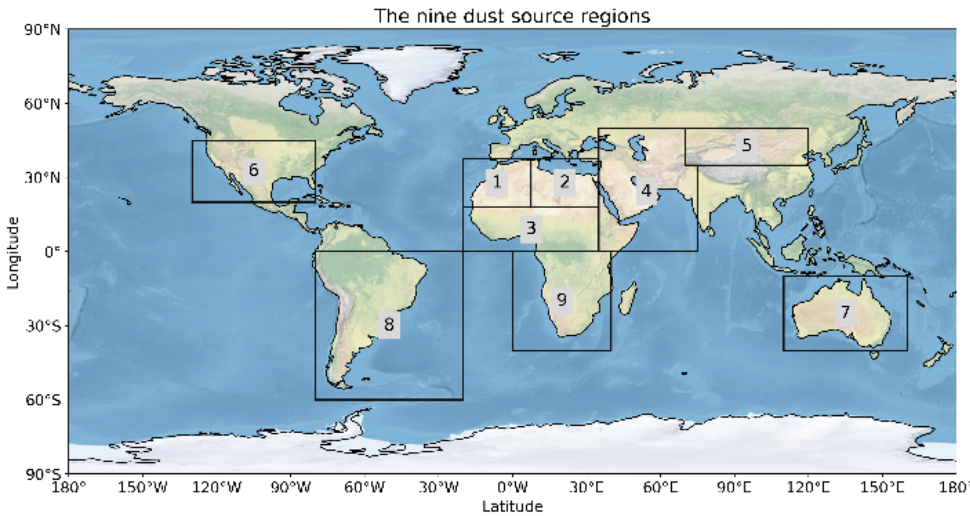

Figure S9. Coordinates of the nine main dust source regions in Kok et al. (2021a) adapted in this study. The coordinates of the nine source regions are: (1) western North Africa (20°W – 7.5°E; 18°N – 37.5°N), (2) eastern North Africa (7.5°E – 35°E; 18°N – 37.5°N), (3) the Sahel (20°W – 35°E; 0°N – 18°N), (4) Middle East / Central Asia (30°E – 70°E for 0°N – 35°N, and 30 – 75°E for 35 – 50°N), (5) East Asia (70°E – 120°E; 35°N – 50°N), (6) North America (130°W – 80°W; 20°N – 45°N), (7) Australia (110°E – 160°E; 10°S – 40°S), (8) South America (80°W – 20°W; 0°S – 60°S), and (9) Southern Africa (0°E – 40°E; 0°S – 40°S). The graph is adopted from (Kok et al., 2021a).

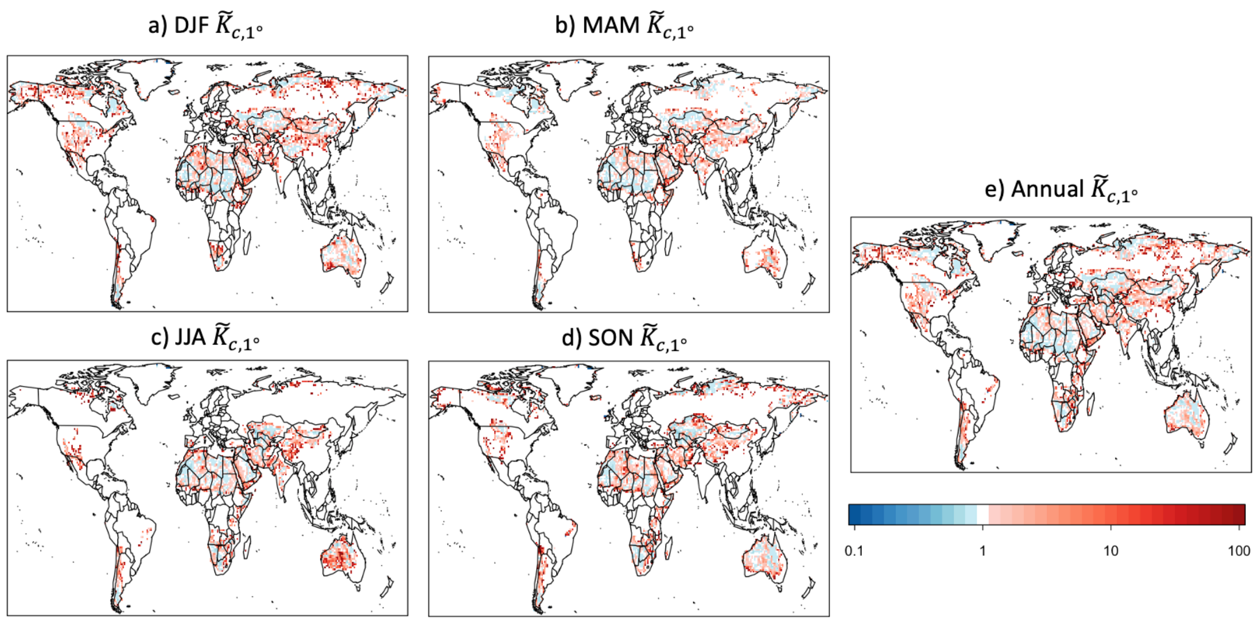

Figure S10. Seasonal variability in the correction map $\widetilde{K}_c$ at a resolution of 0.9°×1.25°, for (a) December–January–February, (b) March–April–May, (c) June–July–August, (d) September–October–November, and (e) the whole year.

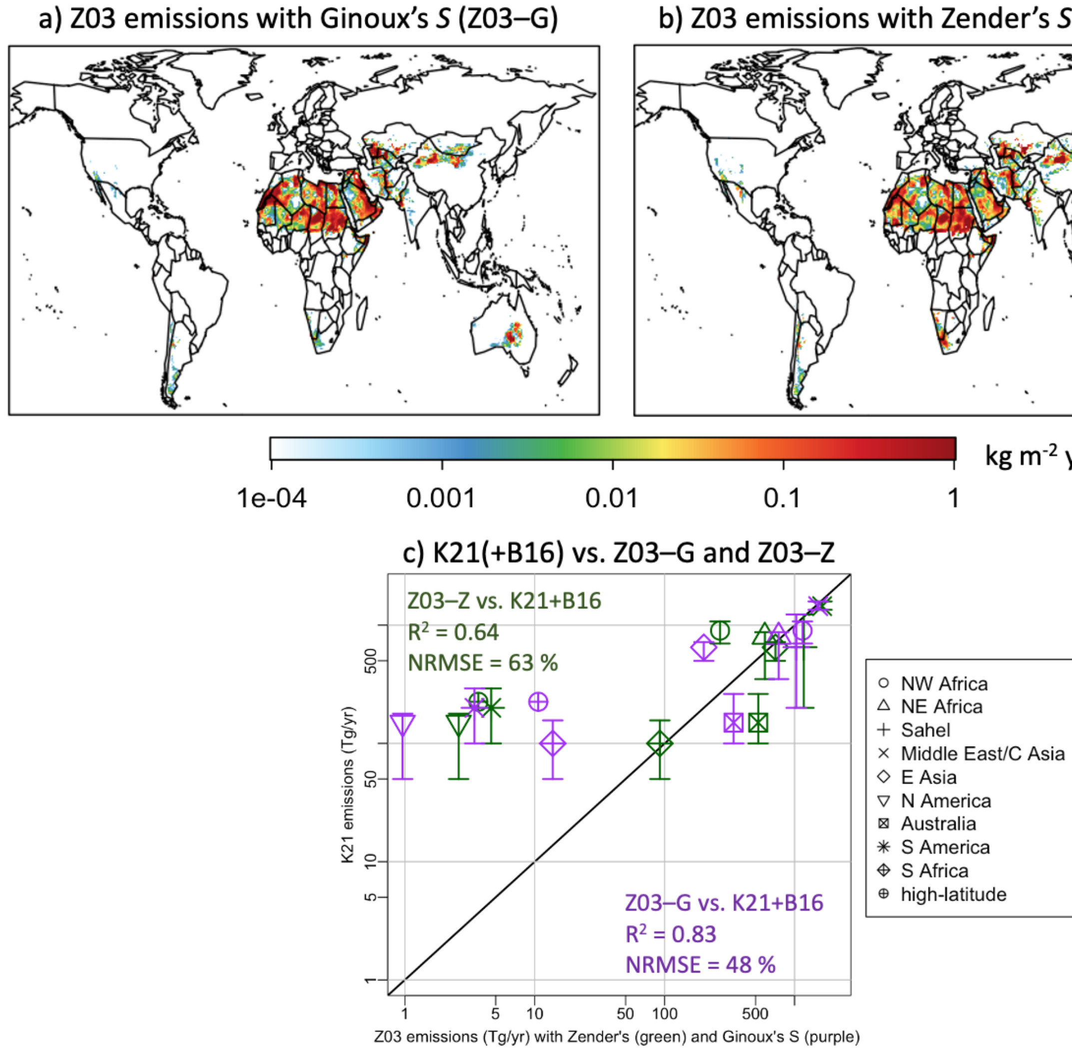

Figure S11. (Kok et al., 2021a, b) DustCOMM emissions versus the dust emission simulations using the (Zender et al., 2003a) scheme with different source functions *S*. (a) Globally gridded Zender et al. (2003a) emissions (kg m^{-2} yr^{-1}) with source function *S* from Ginoux et al. (2001) (Z03–G). (b) Globally gridded Zender et al. (2003a) emissions (kg m^{-2} yr^{-1}) with source function *S* from (Zender et al., 2003b) (Z03–Z). Both (a) and (b) panels are normalized to 5000 Tg yr^{-1} annual global total emissions. (c) Kok et al. (2021a, b) DustCOMM regional emissions (obtained from the fifth column of Table 1 in K21b scaled to a global total of 5000 Tg yr^{-1}) versus the regional emissions computed by the Z03–G scheme and the Z03–Z scheme. The regional emissions are obtained following the nine source regions in Fig. 10a, with one extra point being the "high-latitude" emissions obtained from the Bullard et al. (2016) estimation. The error bars show one standard error, except that the B16 high-latitude emission does not contain any error estimate. The black line shows the 1:1 line.

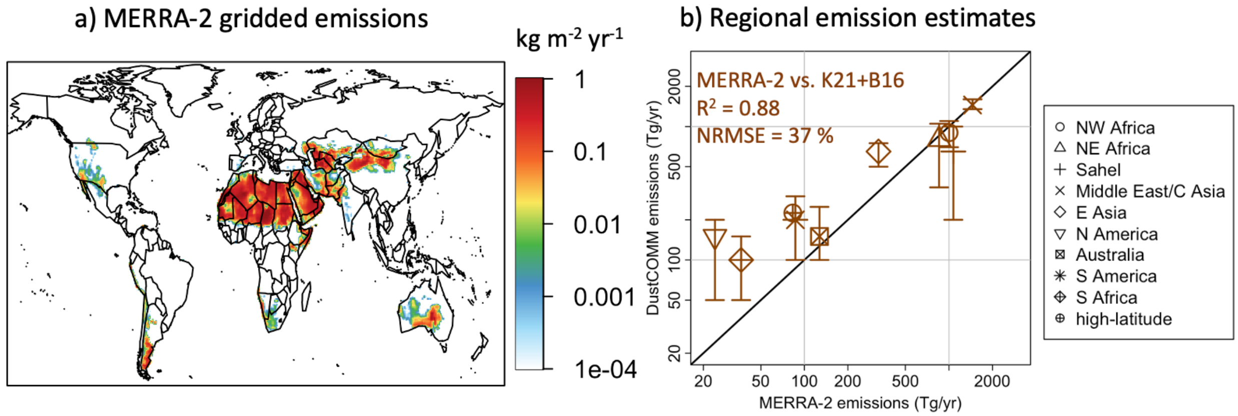

Figure S12. Kok et al. (2021a, b) DustCOMM emissions versus the dust emission simulated by MERRA-2 (Gelaro et al., 2017). (a) Globally gridded MERRA-2 emissions (kg m^{-2} yr^{-1}) using GOCART (Ginoux et al., 2001). Emissions in (a) are normalized to 5000 Tg yr^{-1} annual global total emissions. (c) Kok et al. (2021a, b) DustCOMM regional emissions (obtained from the fifth column of Table 1 in K21b scaled to a global total of 5000 Tg yr^{-1}) versus the regional emissions simulated by MERRA-2. The regional emissions are obtained following the nine source regions in Fig. 10a, with one extra point being the "high-latitude" emissions obtained from the Bullard et al. (2016) estimation. The error bars show one standard error, except that the B16 high-latitude emission does not contain any error estimate. The black line shows the 1:1 line.

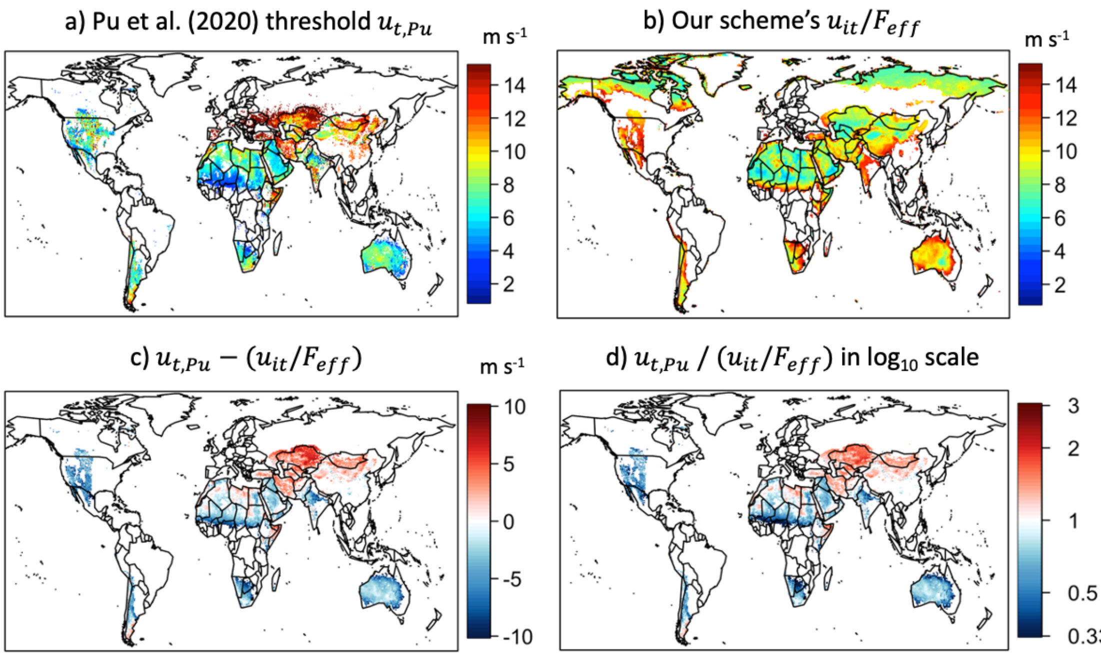

Figure S13. Comparison between the dust emission threshold simulated in this study and the observationally derived dust emission threshold from Pu et al. (2020). (a) Pu et al. (2020) threshold wind speed at 10 m height ($u_{t,Pu}$, m s^{-1}). (b) The simulated impact threshold friction velocity u_{*it} modified by the simulated hybrid drag partition effect, u_{it}/F_{eff} (m s^{-1}), from this study. The impact threshold was translated from a u_{*it} to u_{it} at 10 m height using the log law of the wall. (c) The differences between $u_{t,Pu}$ and u_{it}/F_{eff}. (d) The ratio between the two thresholds, with color bar drawn to $\log_{10}$ scale.

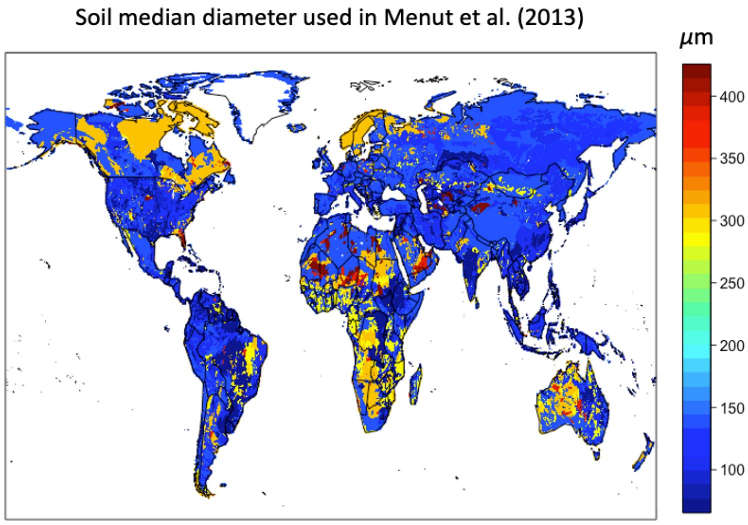

Figure S14. Soil median diameter $\overline{D}_p$ used in Menut et al. (2013) as an input of the CHIMERE chemical transport model, for the dust emission threshold and drag partition effect calculations.

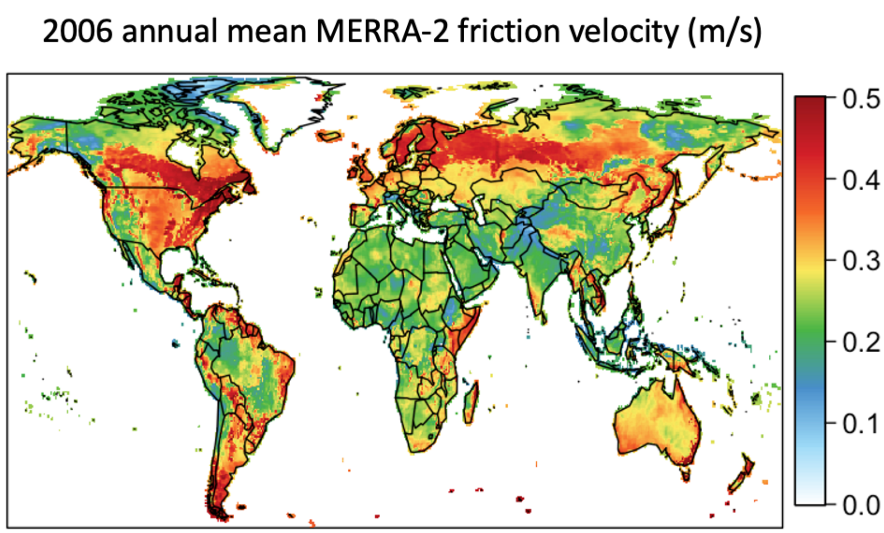

Figure S15. Global distributions of MERRA-2 friction velocity u_* for the year 2006.

References

Andreas, E. L., Claffey, K. J., Jordan, R. E., Fairall, C. W., Guest, P. S., Persson, P. O. G., and Grachev, A. A.: Evaluations of the von Kármán constant in the atmospheric surface layer, Journal of Fluid Mechanics, 559, 117–149, https://doi.org/10.1017/S0022112006000164, 2006.

Appel, K. W., Pouliot, G. A., Simon, H., Sarwar, G., Pye, H. O. T., Napelenok, S. L., Akhtar, F., and Roselle, S. J.: Evaluation of dust and trace metal estimates from the Community Multiscale Air Quality (CMAQ) model version 5.0, Geosci. Model Dev., 6, 883–899, https://doi.org/10.5194/gmd-6-883-2013, 2013.

Appel, K. W., Napelenok, S. L., Foley, K. M., Pye, H. O. T., Hogrefe, C., Luecken, D. J., Bash, J. O., Roselle, S. J., Pleim, J. E., Foroutan, H., Hutzell, W. T., Pouliot, G. A., Sarwar, G., Fahey, K. M., Gantt, B., Gilliam, R. C., Heath, N. K., Kang, D., Mathur, R., Schwede, D. B., Spero, T. L., Wong, D. C., and Young, J. O.: Description and evaluation of the Community Multiscale Air Quality (CMAQ) modeling system version 5.1, Geosci. Model Dev., 10, 1703–1732, https://doi.org/10.5194/gmd-10-1703-2017, 2017.

Bonan, G.: Ecological Climatology: Concepts and Applications, 3rd ed., Cambridge University Press, https://doi.org/10.1017/CBO9781107339200, 2015.

Bullard, J. E., Baddock, M., Bradwell, T., Crusius, J., Darlington, E., Gaiero, D., Gassó, S., Gisladottir, G., Hodgkins, R., McCulloch, R., McKenna-Neuman, C., Mockford, T., Stewart, H., and Thorsteinsson, T.: High-latitude dust in the Earth system, Reviews of Geophysics, 54, 447–485, https://doi.org/10.1002/2016RG000518, 2016.

Cakmur, R. V., Miller, R. L., and Torres, O.: Incorporating the effect of small-scale circulations upon dust emission in an atmospheric general circulation model, Journal of Geophysical Research: Atmospheres, 109, https://doi.org/10.1029/2003JD004067, 2004.

Chandler, D. G., Saxton, K. E., and Busacca, A. J.: Predicting Wind Erodibility of Loessial Soils in the Pacific Northwest by Particle Sizing, Arid Land Research and Management, 19, 13–27, https://doi.org/10.1080/15324980590887074, 2004.

Chatenet, B., Marticorena, B., Gomes, L., and Bergametti, G.: Assessing the microped size distributions of desert soils erodible by wind, Sedimentology, 43, 901–911, https://doi.org/10.1111/j.1365-3091.1996.tb01509.x, 1996.

Chu, C. R., Parlange, M. B., Katul, G. G., and Albertson, J. D.: Probability density functions of turbulent velocity and temperature in the atmospheric surface layer, Water Resources Research, 32, 1681–1688, https://doi.org/10.1029/96WR00287, 1996.

Ciric, V., Manojlovic, M., Nesic, L., and Belic, M.: Soil dry aggregate size distribution: effects of soil type and land use, J. Soil Sci. Plant Nutr., 0–0, https://doi.org/10.4067/S0718-95162012005000025, 2012.

Comola, F., Kok, J. F., Chamecki, M., and Martin, R. L.: The Intermittency of Wind-Driven Sand Transport, Geophysical Research Letters, 46, 13430–13440, https://doi.org/10.1029/2019GL085739, 2019.

Cowie, S. M., Marsham, J. H., and Knippertz, P.: The importance of rare, high-wind events for dust uplift in northern Africa, Geophysical Research Letters, 42, 8208–8215, https://doi.org/10.1002/2015GL065819, 2015.

Darmenova, K., Sokolik, I. N., Shao, Y., Marticorena, B., and Bergametti, G.: Development of a physically based dust emission module within the Weather Research and Forecasting (WRF) model: Assessment of dust emission parameterizations and input parameters for

source regions in Central and East Asia, Journal of Geophysical Research: Atmospheres, 114, https://doi.org/10.1029/2008JD011236, 2009.
Eastham, S. D. and Jacob, D. J.: Limits on the ability of global Eulerian models to resolve intercontinental transport of chemical plumes, Atmospheric Chemistry and Physics, 17, 2543–2553, https://doi.org/10.5194/acp-17-2543-2017, 2017.
FAO/IIASA/ISRIC/ISS-CAS/JRC: Harmonized World Soil Database (version1.2), 2012.
Foroutan, H., Young, J., Napelenok, S., Ran, L., Appel, K. W., Gilliam, R. C., and Pleim, J. E.: Development and evaluation of a physics-based windblown dust emission scheme implemented in the CMAQ modeling system, Journal of Advances in Modeling Earth Systems, 9, 585–608, https://doi.org/10.1002/2016MS000823, 2017.
Gelaro, R., McCarty, W., Suárez, M. J., Todling, R., Molod, A., Takacs, L., Randles, C. A., Darmenov, A., Bosilovich, M. G., Reichle, R., Wargan, K., Coy, L., Cullather, R., Draper, C., Akella, S., Buchard, V., Conaty, A., Silva, A. M. da, Gu, W., Kim, G.-K., Koster, R., Lucchesi, R., Merkova, D., Nielsen, J. E., Partyka, G., Pawson, S., Putman, W., Rienecker, M., Schubert, S. D., Sienkiewicz, M., and Zhao, B.: The Modern-Era Retrospective Analysis for Research and Applications, Version 2 (MERRA-2), Journal of Climate, 30, 5419–5454, https://doi.org/10.1175/JCLI-D-16-0758.1, 2017.
Ginoux, P., Chin, M., Tegen, I., Prospero, J. M., Holben, B., Dubovik, O., and Lin, S.-J.: Sources and distributions of dust aerosols simulated with the GOCART model, Journal of Geophysical Research: Atmospheres, 106, 20255–20273, https://doi.org/10.1029/2000JD000053, 2001.
Grini, A., Myhre, G., Zender, C. S., and Isaksen, I. S. A.: Model simulations of dust sources and transport in the global atmosphere: Effects of soil erodibility and wind speed variability, Journal of Geophysical Research: Atmospheres, 110, https://doi.org/10.1029/2004JD005037, 2005.
Hengl, T., Jesus, J. M. de, Heuvelink, G. B. M., Gonzalez, M. R., Kilibarda, M., Blagotić, A., Shangguan, W., Wright, M. N., Geng, X., Bauer-Marschallinger, B., Guevara, M. A., Vargas, R., MacMillan, R. A., Batjes, N. H., Leenaars, J. G. B., Ribeiro, E., Wheeler, I., Mantel, S., and Kempen, B.: SoilGrids250m: Global gridded soil information based on machine learning, PLOS ONE, 12, e0169748, https://doi.org/10.1371/journal.pone.0169748, 2017.
Hillel, D.: Fundamentals of Soil Physics, Elsevier, https://doi.org/10.1016/C2009-0-03109-2, 1980.
Jiménez, P. A., Dudhia, J., and Navarro, J.: On the surface wind speed probability density function over complex terrain, Geophysical Research Letters, 38, https://doi.org/10.1029/2011GL049669, 2011.
Kalhoro, S. A., Xu, X., Chen, W., Hua, R., Raza, S., and Ding, K.: Effects of Different Land-Use Systems on Soil Aggregates: A Case Study of the Loess Plateau (Northern China), Sustainability, 9, 1349, https://doi.org/10.3390/su9081349, 2017.
Klein Goldewijk, K., Beusen, A., Doelman, J., and Stehfest, E.: Anthropogenic land use estimates for the Holocene – HYDE 3.2, Earth Syst. Sci. Data, 9, 927–953, https://doi.org/10.5194/essd-9-927-2017, 2017.
Klose, M., Gill, T. E., Webb, N. P., and Van Zee, J. W.: Field sampling of loose erodible material: A new system to consider the full particle-size spectrum, Aeolian Research, 28, 83–90, https://doi.org/10.1016/j.aeolia.2017.08.003, 2017.

Klose, M., Jorba, O., Gonçalves Ageitos, M., Escribano, J., Dawson, M. L., Obiso, V., Di Tomaso, E., Basart, S., Montané Pinto, G., Macchia, F., Ginoux, P., Guerschman, J., Prigent, C., Huang, Y., Kok, J. F., Miller, R. L., and Pérez García-Pando, C.: Mineral dust cycle in the Multiscale Online Nonhydrostatic AtmospheRe CHemistry model (MONARCH) Version 2.0, Geosci. Model Dev., 14, 6403–6444, https://doi.org/10.5194/gmd-14-6403-2021, 2021.

Kok, J. F., Mahowald, N. M., Fratini, G., Gillies, J. A., Ishizuka, M., Leys, J. F., Mikami, M., Park, M.-S., Park, S.-U., Van Pelt, R. S., and Zobeck, T. M.: An improved dust emission model – Part 1: Model description and comparison against measurements, Atmospheric Chemistry and Physics, 14, 13023–13041, https://doi.org/10.5194/acp-14-13023-2014, 2014a.

Kok, J. F., Albani, S., Mahowald, N. M., and Ward, D. S.: An improved dust emission model – Part 2: Evaluation in the Community Earth System Model, with implications for the use of dust source functions, Atmospheric Chemistry and Physics, 14, 13043–13061, https://doi.org/10.5194/acp-14-13043-2014, 2014b.

Kok, J. F., Adebiyi, A. A., Albani, S., Balkanski, Y., Checa-Garcia, R., Chin, M., Colarco, P. R., Hamilton, D. S., Huang, Y., Ito, A., Klose, M., Leung, D. M., Li, L., Mahowald, N. M., Miller, R. L., Obiso, V., Pérez García-Pando, C., Rocha-Lima, A., Wan, J. S., and Whicker, C. A.: Improved representation of the global dust cycle using observational constraints on dust properties and abundance, Atmos. Chem. Phys., 21, 8127–8167, https://doi.org/10.5194/acp-21-8127-2021, 2021a.

Kok, J. F., Adebiyi, A. A., Albani, S., Balkanski, Y., Checa-Garcia, R., Chin, M., Colarco, P. R., Hamilton, D. S., Huang, Y., Ito, A., Klose, M., Li, L., Mahowald, N. M., Miller, R. L., Obiso, V., Pérez García-Pando, C., Rocha-Lima, A., and Wan, J. S.: Contribution of the world's main dust source regions to the global cycle of desert dust, Atmos. Chem. Phys., 21, 8169–8193, https://doi.org/10.5194/acp-21-8169-2021, 2021b.

Kutzbach, J., Bonan, G., Foley, J., and Harrison, S. P.: Vegetation and soil feedbacks on the response of the African monsoon to orbital forcing in the early to middle Holocene, Nature, 384, 623–626, https://doi.org/10.1038/384623a0, 1996.

Laurent, B., Marticorena, B., Bergametti, G., Léon, J. F., and Mahowald, N. M.: Modeling mineral dust emissions from the Sahara desert using new surface properties and soil database, J. Geophys. Res., 113, D14218, https://doi.org/10.1029/2007JD009484, 2008.

Lee, T. R. and Buban, M.: Evaluation of Monin–Obukhov and Bulk Richardson Parameterizations for Surface–Atmosphere Exchange, Journal of Applied Meteorology and Climatology, 59, 1091–1107, https://doi.org/10.1175/JAMC-D-19-0057.1, 2020.

Li, X., Feng, G., Sharratt, B. S., Zheng, Z., Pi, H., and Gao, F.: Soil Wind Erodibility Based on Dry Aggregate-Size Distribution in the Tarim Basin, Soil Science Society of America Journal, 78, 2009–2016, https://doi.org/10.2136/sssaj2014.06.0235, 2014.

Liu, L., Wang, J., Li, X., Liu, Y., Ta, W., and Peng, H.: Determination of erodible particles on cultivated soils by wind tunnel simulation, Chin. Sci. Bull., 43, 1646–1651, https://doi.org/10.1007/BF02883411, 1998.

Mahowald, N. M., Muhs, D. R., Levis, S., Rasch, P. J., Yoshioka, M., Zender, C. S., and Luo, C.: Change in atmospheric mineral aerosols in response to climate: Last glacial period, preindustrial, modern, and doubled carbon dioxide climates, Journal of Geophysical Research: Atmospheres, 111, https://doi.org/10.1029/2005JD006653, 2006.

Mailler, S., Menut, L., Khvorostyanov, D., Valari, M., Couvidat, F., Siour, G., Turquety, S., Briant, R., Tuccella, P., Bessagnet, B., Colette, A., Létinois, L., Markakis, K., and Meleux, F.: CHIMERE-2017: from urban to hemispheric chemistry-transport modeling, Geoscientific Model Development, 10, 2397–2423, https://doi.org/10.5194/gmd-10-2397-2017, 2017.

Malobane, M. E., Nciizah, A. D., Mudau, F. N., and Wakindiki, I. I. C.: Discrimination of soil aggregates using micro-focus X-ray computed tomography in a five-year-old no-till natural fallow and conventional tillage in South Africa, Heliyon, 5, e01819, https://doi.org/10.1016/j.heliyon.2019.e01819, 2019.

Marticorena, B. and Bergametti, G.: Modeling the atmospheric dust cycle: 1. Design of a soil-derived dust emission scheme, Journal of Geophysical Research: Atmospheres, 100, 16415–16430, https://doi.org/10.1029/95JD00690, 1995.

Marticorena, B., Kardous, M., Bergametti, G., Callot, Y., Chazette, P., Khatteli, H., Hégarat-Mascle, S. L., Maillé, M., Rajot, J.-L., Vidal-Madjar, D., and Zribi, M.: Surface and aerodynamic roughness in arid and semiarid areas and their relation to radar backscatter coefficient, Journal of Geophysical Research: Earth Surface, 111, https://doi.org/10.1029/2006JF000462, 2006.

Martin, R. L. and Kok, J. F.: Distinct Thresholds for the Initiation and Cessation of Aeolian Saltation From Field Measurements, Journal of Geophysical Research: Earth Surface, 123, 1546–1565, https://doi.org/10.1029/2017JF004416, 2018.

Mei, F., Zhang, X., Lu, H., Shen, Z., and Wang, Y.: Characterization of MASDs of surface soils in north China and its influence on estimating dust emission, Chin.Sci.Bull., 49, 2169–2176, https://doi.org/10.1007/BF03185784, 2004.

Meng, J., Martin, R. V., Ginoux, P., Hammer, M., Sulprizio, M. P., Ridley, D. A., and van Donkelaar, A.: Grid-independent high-resolution dust emissions (v1.0) for chemical transport models: application to GEOS-Chem (12.5.0), Geoscientific Model Development, 14, 4249–4260, https://doi.org/10.5194/gmd-14-4249-2021, 2021.

Menut, L.: Modeling of Mineral Dust Emissions with a Weibull Wind Speed Distribution Including Subgrid-Scale Orography Variance, Journal of Atmospheric and Oceanic Technology, 35, 1221–1236, https://doi.org/10.1175/JTECH-D-17-0173.1, 2018.

Menut, L., Pérez, C., Haustein, K., Bessagnet, B., Prigent, C., and Alfaro, S.: Impact of surface roughness and soil texture on mineral dust emission fluxes modeling, Journal of Geophysical Research: Atmospheres, 118, 6505–6520, https://doi.org/10.1002/jgrd.50313, 2013.

Menut, L., Bessagnet, B., Briant, R., Cholakian, A., Couvidat, F., Mailler, S., Pennel, R., Siour, G., Tuccella, P., Turquety, S., and Valari, M.: The CHIMERE v2020r1 online chemistry-transport model, Geoscientific Model Development, 14, 6781–6811, https://doi.org/10.5194/gmd-14-6781-2021, 2021.

Mirzamostafa, N., Stone, L. R., Hagen, L. J., and Skidmore, E. L.: Soil Aggregate and Texture Effects on Suspension Components from Wind Erosion, Soil Science Society of America Journal, 62, 1351–1361, https://doi.org/10.2136/sssaj1998.03615995006200050030x, 1998.

Okin, G. S.: A new model of wind erosion in the presence of vegetation, Journal of Geophysical Research: Earth Surface, 113, https://doi.org/10.1029/2007JF000758, 2008.

Oleson, K., Lawrence, D., Bonan, G., Drewniack, B., Huang, M., Koven, C., Levis, S., Li, F., Riley, W., and Subin, Z.: Technical description of version 4.5 of the Community Land

Model (CLM)(Technical Note No. NCAR/TN-503+ STR). Boulder, CO: National Center for Atmospheric Research Earth System Laboratory, 2013.

Prigent, C., Tegen, I., Aires, F., Marticorena, B., and Zribi, M.: Estimation of the aerodynamic roughness length in arid and semi-arid regions over the globe with the ERS scatterometer, Journal of Geophysical Research: Atmospheres, 110, https://doi.org/10.1029/2004JD005370, 2005.

Prigent, C., Jiménez, C., and Catherinot, J.: Comparison of satellite microwave backscattering (ASCAT) and visible/near-infrared reflectances (PARASOL) for the estimation of aeolian aerodynamic roughness length in arid and semi-arid regions, Atmospheric Measurement Techniques, 5, 2703–2712, https://doi.org/10.5194/amt-5-2703-2012, 2012.

Pu, B., Ginoux, P., Guo, H., Hsu, N. C., Kimball, J., Marticorena, B., Malyshev, S., Naik, V., O'Neill, N. T., Pérez García-Pando, C., Paireau, J., Prospero, J. M., Shevliakova, E., and Zhao, M.: Retrieving the global distribution of the threshold of wind erosion from satellite data and implementing it into the Geophysical Fluid Dynamics Laboratory land–atmosphere model (GFDL AM4.0/LM4.0), Atmos. Chem. Phys., 20, 55–81, https://doi.org/10.5194/acp-20-55-2020, 2020.

Rastigejev, Y., Park, R., Brenner, M. P., and Jacob, D. J.: Resolving intercontinental pollution plumes in global models of atmospheric transport, Journal of Geophysical Research: Atmospheres, 115, https://doi.org/10.1029/2009JD012568, 2010.

Raupach, M. R., Gillette, D. A., and Leys, J. F.: The effect of roughness elements on wind erosion threshold, Journal of Geophysical Research: Atmospheres, 98, 3023–3029, https://doi.org/10.1029/92JD01922, 1993.

Ridley, D. A., Heald, C. L., Pierce, J. R., and Evans, M. J.: Toward resolution-independent dust emissions in global models: Impacts on the seasonal and spatial distribution of dust, Geophysical Research Letters, 40, 2873–2877, https://doi.org/10.1002/grl.50409, 2013.

Semakin, A. N. and Rastigejev, Y.: Numerical Simulation of Global-Scale Atmospheric Chemical Transport with High-Order Wavelet-Based Adaptive Mesh Refinement Algorithm, Monthly Weather Review, 144, 1469–1486, https://doi.org/10.1175/MWR-D-15-0200.1, 2016.

Shao, Y., Raupach, M. R., and Findlater, P. A.: Effect of saltation bombardment on the entrainment of dust by wind, Journal of Geophysical Research: Atmospheres, 98, 12719–12726, https://doi.org/10.1029/93JD00396, 1993.

Shao, Y., Ishizuka, M., Mikami, M., and Leys, J. F.: Parameterization of size-resolved dust emission and validation with measurements, Journal of Geophysical Research: Atmospheres, 116, https://doi.org/10.1029/2010JD014527, 2011.

Shirazi, M. A. and Boersma, L.: A Unifying Quantitative Analysis of Soil Texture, Soil Science Society of America Journal, 48, 142–147, https://doi.org/10.2136/sssaj1984.03615995004800010026x, 1984.

Stull, R.: An Introduction to Boundary Layer Meteorology, 1988.

Su, Y., Wang, F., Zhang, Z., and Du, M.: Soil Properties and Characteristics of Soil Aggregate in Marginal Farmlands of Oasis in the Middle of Hexi Corridor Region, Northwest China, Agricultural Sciences in China, 6, 706–714, https://doi.org/10.1016/S1671-2927(07)60103-5, 2007.

Swet, N. and Katra, I.: Reduction in soil aggregation in response to dust emission processes, Geomorphology, 268, 177–183, https://doi.org/10.1016/j.geomorph.2016.06.002, 2016.

Tai, A. P. K., Ma, P. H. L., Chan, Y.-C., Chow, M.-K., Ridley, D. A., and Kok, J. F.: Impacts of climate and land cover variability and trends on springtime East Asian dust emission over 1982–2010: A modeling study, Atmospheric Environment, 254, 118348, https://doi.org/10.1016/j.atmosenv.2021.118348, 2021.

Tegen, I., Harrison, S. P., Kohfeld, K., Prentice, I. C., Coe, M., and Heimann, M.: Impact of vegetation and preferential source areas on global dust aerosol: Results from a model study, Journal of Geophysical Research: Atmospheres, 107, AAC 14-1-AAC 14-27, https://doi.org/10.1029/2001JD000963, 2002.

Udom, B. E. and Ogunwole, J. O.: Soil organic carbon, nitrogen, and phosphorus distribution in stable aggregates of an Ultisol under contrasting land use and management history, Journal of Plant Nutrition and Soil Science, 178, 460–467, https://doi.org/10.1002/jpln.201400535, 2015.

Wagner, L. E., Ambe, N. M., and Barnes, P.: Tillage-Induced Soil Aggregate Status as Influenced by Water Content, Transactions of the ASAE, 35, 499–504, https://doi.org/10.13031/2013.28627, 1992.

Zender, C. S., Bian, H., and Newman, D.: Mineral Dust Entrainment and Deposition (DEAD) model: Description and 1990s dust climatology, Journal of Geophysical Research: Atmospheres, 108, https://doi.org/10.1029/2002JD002775, 2003a.

Zender, C. S., Newman, D., and Torres, O.: Spatial heterogeneity in aeolian erodibility: Uniform, topographic, geomorphic, and hydrologic hypotheses, Journal of Geophysical Research: Atmospheres, 108, https://doi.org/10.1029/2002JD003039, 2003b.

Zhang, K., Zhao, C., Wan, H., Qian, Y., Easter, R. C., Ghan, S. J., Sakaguchi, K., and Liu, X.: Quantifying the impact of sub-grid surface wind variability on sea salt and dust emissions in CAM5, Geoscientific Model Development, 9, 607–632, https://doi.org/10.5194/gmd-9-607-2016, 2016.

Zhang, L., Kok, J. F., Henze, D. K., Li, Q., and Zhao, C.: Improving simulations of fine dust surface concentrations over the western United States by optimizing the particle size distribution, Geophysical Research Letters, 40, 3270–3275, https://doi.org/10.1002/grl.50591, 2013.

Zhuang, J., Jacob, D. J., and Eastham, S. D.: The importance of vertical resolution in the free troposphere for modeling intercontinental plumes, Atmospheric Chemistry and Physics, 18, 6039–6055, https://doi.org/10.5194/acp-18-6039-2018, 2018.

Zhuang, J., Kochkov, D., Bar-Sinai, Y., Brenner, M. P., and Hoyer, S.: Learned discretizations for passive scalar advection in a two-dimensional turbulent flow, Phys. Rev. Fluids, 6, 064605, https://doi.org/10.1103/PhysRevFluids.6.064605, 2021.